

# Development of a bioengineered tissue model and its application in the investigation of the depth selectivity of polarization gating

Yang Liu, Young L. Kim, and Vadim Backman

Understanding the propagation of polarized light in tissue is crucial for a number of biomedical optics applications. Here we report the development of a bioengineered connective tissue model fabricated by the combination of scaffolding and cross-linking techniques to study light transport in biological tissue. It demonstrates great similarity to real connective tissue in its optical properties as well as microarchitecture. Moreover, the optical properties of the model can be reproducibly controlled. As an example, we report the utilization of this model to study the effect of epithelium and the underlying connective tissue on the depth selectivity of polarization gating. © 2005 Optical Society of America

OCIS codes: 170.3660, 260.5430, 290.1350.

## 1. Introduction

There has been a significant interest in using elastic light-scattering techniques to probe the organization of biological tissue.<sup>1–11</sup> Because most biological tissues have a multilayered structure, depth-resolved measurements are crucial. Typically, photons propagating in superficial tissue experience only single-scattering and low-order scattering events, whereas photons propagating deeper into the tissue scatter multiple times and eventually become almost completely randomized in direction (e.g., diffuse scattering). In most cancerous and precancerous detection, the diagnostic information must be obtained from the most superficial tissue because it is the origin of more than 85% of human cancers. Epithelia are relatively thin (typically less than a couple of hundreds of micrometers thick), avascular, highly cellular tissue lining the internal surfaces of the body. Because the majority of photons returned from a tissue penetrate several millimeters below the surface, distinguishing between light returned from the superficial tissue and deeper tissue requires specialized techniques.

Polarization gating has been used to differentiate

between single scattering and multiple scattering to probe the superficial tissue on the basis of the fact that multiple scattering depolarizes light. In polarization gating, a tissue is illuminated by a polarized light, and the returned elastic scattering signal is split into two components with polarizations parallel (copolarized signal) and orthogonal (cross-polarized signal) to that of the incident light. One can increase the sensitivity of the scattered light to near-surface structures by rejecting the depolarized light. For example, Jacques *et al.* achieved the imaging of superficially located structures of the skin by means of measuring the degree of polarization of the returned light.<sup>12,13</sup> Moreover, the spectral analysis of the differential polarization component was used to obtain quantitative information about the morphology of superficial epithelial cells.<sup>3,9,14–18</sup> Backman *et al.*<sup>15</sup> and Sokolov *et al.*<sup>8</sup> showed that a differential polarization signal (i.e., the difference between the co- and cross-polarized components of the scattered light) is primarily sensitive to the optical properties of the superficial tissue. Mourant *et al.*<sup>10</sup> and Johnson and Mourant<sup>18</sup> showed that both the spectrum and the angular distributions of polarized backscattering measurements are sensitive to the size of scatterers in tissue phantoms and the biological tissues. Furthermore, Kim *et al.*<sup>11</sup> and Roy *et al.*<sup>19</sup> showed that the comprehensive analysis of the spectral, scattering angle, and azimuthal properties of the differential polarization signal has the potential to detect the earliest preneoplastic changes in colonic epithelium.

Such significant interest in polarization-gating

---

The authors are with the Department of Biomedical Engineering, Northwestern University, Evanston, Illinois 60208. The e-mail address of Y. Liu is yangliu@northwestern.edu.

Received 17 June 2004; revised manuscript received 8 October 2004; accepted 15 October 2004.

0003-6935/05/122288-12\$15.00/0

© 2005 Optical Society of America

techniques is underlined by the relative simplicity of this approach. Compared with other depth-resolved techniques,<sup>7,20–26</sup> polarization gating is one of the most inexpensive approaches. Moreover, it can provide spectroscopic and angle-resolved information about tissue scattering and allows *in vivo* implementation. However, the propagation of polarized light in biological tissue remains one of the least understood phenomena in tissue optics. Thus understanding the propagation of polarized light in tissue is of critical importance. However, as discussed below, these investigations have been impeded in part by the lack of realistic tissue models that can replicate both the morphological complexity and the optical properties of biological tissue.

Several crucial questions remain unanswered: Which tissue characteristics determine the penetration depth? Although evidence exists that the differential polarization signal, as well as the degree of polarization, is sensitive to superficial tissue, the depth of penetration has not been quantified. How does the penetration depth of the differential polarization signal depend on the optical properties of the superficial tissue and deeper tissue? The role of superficial epithelium and the effect of underlying connective tissue in polarization gating are still poorly understood. Possible explanations have been proposed by several investigators. According to one explanation, polarization gating is due to the depolarization of the incident light, which primarily occurs in the randomly birefringent connective tissue layer underlying the epithelium, whereas the contribution of the epithelium is much smaller.<sup>13</sup> Thus the epithelium does not determine the penetration depth and affects only the spectral properties of the polarization-gated signal. In this explanation, the penetration depth should typically include the entire epithelium plus a thin uppermost portion of the connective tissue. Alternatively, it was suggested that the epithelium and connective tissue have similar light-depolarizing properties. According to another explanation, the penetration depth depends primarily on the optical thickness of a tissue,<sup>14</sup> regardless of tissue type (e.g., polarization gating is due to out-of-plane scattering of polarized light rather than the depolarization of the incident light *per se*).

The dearth of knowledge about the mechanisms of polarization gating is in part due to the lack of suitable tissue models. Evidently, there is no substitute for a living mucosal tissue. However, the use of living tissues in polarization-gating experiments suffers from several drawbacks. Most importantly, the optical and physical properties of a living tissue cannot be varied or controlled in a predictable manner, which is crucial for repeatable, reproducible, and well-controlled experiments. Moreover, it is sometimes difficult to separate the epithelium and the connective tissue layers. Finally, in polarization-gating experiments with living tissue, distinguishing the depth from which polarization-gated photons emerge is not trivial.

Tissue models (also known as tissue phantoms)

give the advantage of easy and good control over the optical parameters of the tissue. Aqueous solutions of polystyrene microspheres and Intralipid suspension have been and still remain the most frequently used tissue phantoms.<sup>27</sup> However, the relevance of such models to study light transport in tissue has been questioned. The major drawback of these models is that they are not capable of representing the complexity of tissue organization: A suspension of isolated spherical particles of a more or less uniform size is hardly a good representation of a tissue whose scattering structures may range from nearly spherical intracellular structures to highly elongated collagen fibers, covering length scales resulting from near-field to far-field interactions. Indeed, Sankaran and colleagues<sup>28–30</sup> have shown that the polarized light propagation in biological tissues in the forward direction behaves differently from the propagation in tissue phantoms consisting of a suspension of polystyrene microspheres. The same investigators found that the scattering properties of biological tissue are better modeled by closely spaced rather than isolated particles. Although no data exist showing that in the backward direction this effect plays a similarly important role, the research of Sankaran and colleagues clearly underlines the necessity to develop more realistic tissue models.

Several investigators have developed tissue models for biomedical optics applications. Sokolov *et al.* modeled stroma to study tissue fluorescence. The fluorescence signals obtained from their phantoms showed excellent similarity to the fluorescence from living cervical tissue.<sup>31</sup> Zoumi *et al.* have developed the organotypic raft tissue model and extracted its optical properties by use of second-harmonic-generation imaging.<sup>32</sup> Marquez *et al.* have successfully developed a tissue-simulating optical phantom and studied its optical properties.<sup>33</sup> However, no tissue model has been designed to study the propagation of elastically scattered polarized light in superficial tissues such as mucosae.

In this paper we report the development of a bioengineered connective tissue model specifically designed to study light transport in biological tissue. We demonstrate excellent similarity between the optical and the morphological properties of this model and those of real connective tissue. We show that this model can be used as a basis for fabrication of more complex multilayered tissue phantoms. Moreover, the physical and optical properties of the model can be easily and reproducibly controlled.

This paper is organized as follows. In Section 2 we discuss the fabrication of the tissue model. In Section 3 we discuss the characterization of the microarchitecture of the tissue model by using scanning electron microscopy (SEM) and its comparison with that of mucosal connective tissue. In Section 4 we characterize the optical properties of the tissue model by using the integrating-sphere technique. In Section 5 the effect of epithelium and the underlying connective tissue on the depth selectivity of polarization gating

is investigated. Finally, Section 6 summarizes the results reported in this paper.

## 2. Fabrication of a Bioengineered Connective Tissue Model

An ideal tissue model should have the microarchitecture and optical properties sufficiently similar to those of a real tissue. Moreover, the physical and optical properties of the model should be controllable in the process of its fabrication. In this section we discuss the development of a bioengineered tissue model that possesses these properties. Because collagen is the ubiquitous element in connective tissue,<sup>34</sup> it was chosen as the major building block of the bioengineered connective tissue model. The model was fabricated by the combination of scaffolding and cross-linking techniques that have been widely used in tissue engineering.<sup>35</sup>

The preparation of a bioengineered connective tissue phantom consists of two main steps—the preparation of a collagen gel and its transformation to a cross-linked collagen scaffold. All chemicals were purchased from Sigma-Aldrich. To prepare the collagen solution, we mixed eight parts of a 2.9-mg/ml collagen solution (Vitrogen, Cohesion Technologies) with one part of 10× phosphate-buffered saline solution and one part of 0.2-M Hepes. The pH of the solution was adjusted to  $7.4 \pm 0.2$  by addition of a few drops of 1-M NaOH and monitored by phenol red. Furthermore, to fabricate a model with a nonzero absorption coefficient, one can add the hemoglobin (Aldrich-Sigma) and mix it with the collagen solution. The collagen solution was poured into a chamber mold and gelled by incubation of the neutralized solution at 37 °C for 1 h. We fabricated the collagen scaffold by freezing the collagen gel at  $-78$  °C for 1 h and then freeze-dried it under high vacuum ( $60 \times 10^{-3}$  mBar) overnight. The collagen scaffold was cross-linked by a glutaraldehyde solution for 1 h. The cross-linked scaffold was washed in distilled water.

We note several advantages of the developed tissue model. First, the optical and physical properties of the model can be adjusted within a wide range (Fig. 1). One can easily control the physical thickness of the tissue model by varying the initial volume of the collagen solution poured into the mold. Owing to the fact that tissue models with higher collagen fiber densities tend to have higher scattering coefficients, the scattering coefficient is approximately proportional to the concentration of the cross-linking agent, the glutaraldehyde solution. Moreover, because less porous models tend to have a lower anisotropy factor, one can control the anisotropy factor  $g$  by varying the freeze-drying pressure. Specifically, a tissue model fabricated with a high drying pressure has a larger  $g$  than that fabricated with a low drying pressure. Finally, one can adjust the absorption coefficient by varying the concentration of hemoglobin. Figure 1 shows the dependence of the glutaraldehyde concentration on the scattering coefficient ( $\lambda = 632.8$  nm), the dependence of the anisotropy factor on the freeze-

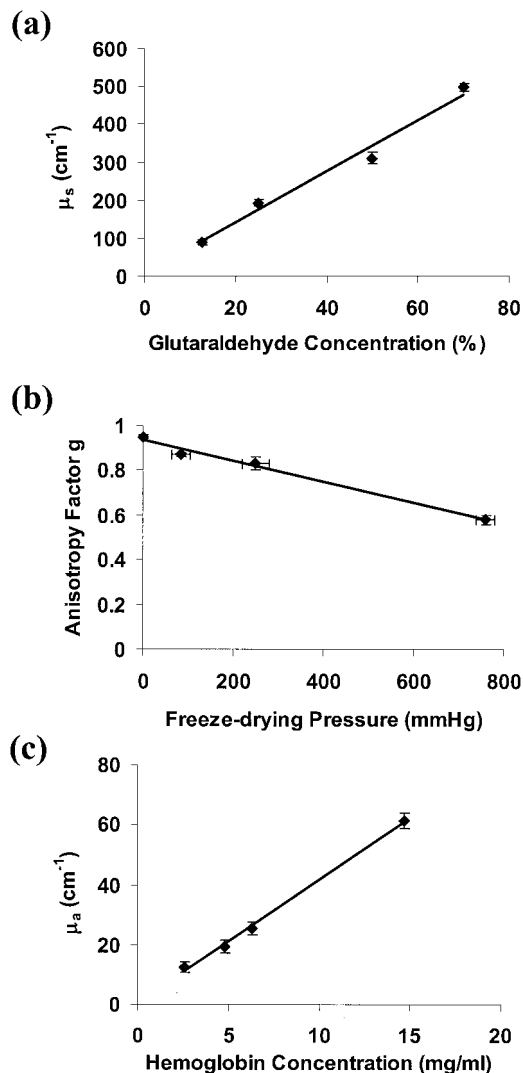


Fig. 1. One can control optical properties of the tissue model by varying synthesis conditions. (a) The dependence of the scattering coefficient  $\mu_s(\lambda = 632.8$  nm) on the concentration of the glutaraldehyde solution. (b) The dependence of the anisotropy factor  $g(\lambda = 632.8$  nm) on the freeze-drying pressure. (c) The dependence of the absorption coefficient  $\mu_a(\lambda = 543.5$  nm) on the concentration of the hemoglobin solution.

drying pressure, and the dependence of the absorption coefficient on the hemoglobin concentration ( $\lambda = 543.5$  nm). Second, we found that the optical properties and thickness of the model are reproducible. To show this, we fabricated several ( $n = 8$ ) tissue models following the same procedure. The optical properties, i.e., the scattering coefficient, reduced scattering coefficients, and the anisotropy parameter, and thickness of the models were measured, and the standard deviations of all these characteristics were found to be within 8% of the respective means. Finally, the tissue model can be kept in water at room temperature for over 6 months without any appreciable changes in its optical properties, which further facilitates utilization of this model in practice. In the following sections we show that the microarchitec-

ture and optical properties of this model are similar to those of connective tissue.

### 3. Characterization of the Microarchitecture of the Bioengineered Tissue Model

#### A. Sample Preparation for Scanning Electron Microscopy

In this section we show that the microarchitecture of the bioengineered tissue model introduced in Section 2 is sufficiently similar to that of real connective tissue. To compare the microarchitecture of the bioengineered connective tissue model with that of real mucosal connective tissue, SEM images were obtained from both tissue models ( $n = 30$ ) and rat colonic connective tissue ( $n = 20$ ). Rat colonic tissue is a typical example of mucosal–submucosal tissue lining the inner surfaces of the majority of organs. There has been significant interest in using optical techniques to detect precancerous lesions and other pathological conditions in the mucosae–submucosae. The reason for such interest is twofold: (1) carcinomas arising in the mucosae are responsible for the absolute majority of human cancers, and (2) these tissues can be optically interrogated in a relatively easy manner, and this approach may lead to the early detection of this disease at a premalignant stage.<sup>11,15,16,25</sup> All samples were identically prepared following the standard SEM protocol. In brief, the sample (either a model or the rat colon tissue) was fixed with 2.5% glutaraldehyde solution at 4 °C overnight. The fixed sample was frozen at  $-78$  °C for over 1 h and freeze dried overnight. The dried sample was coated with 3-nm-thick gold with a sputter coater, and the SEM images were taken with Hitachi S-3500N VP SEM (Electron Probe Instrumentation Center, Northwestern University). Although the fixation and freeze-drying procedure of SEM was used to preserve the original morphology of the sample, certain SEM artifacts are unavoidable. The fixation with glutaraldehyde may cause minor loss of cellular materials and the contraction of extracellular space.<sup>36</sup> The freeze-drying procedure may cause slight shrinkage of the sample: approximately 7% shrinkage of the entire cell<sup>37</sup> and as much as 20% shrinkage of relatively large tissue structures.<sup>38</sup> However, in that electron microscope images of both rat colonic tissues and tissue models were prepared following exactly the same procedure, the slight tissue shrinkage does not affect the comparison of the two.

#### B. Comparison of the Microstructure of the Tissue Model and Connective Tissue

Figure 2 shows two representative SEM images obtained from (a) rat colonic connective tissue and (b) a bioengineered connective tissue model. These SEM images show significant structural similarity between the bioengineered connective tissue model and the colon connective tissue. As evident from the SEM images, in both the colonic connective tissue and the model, the major structural components are collagen fibers and fiber bundles. Both the colon connective

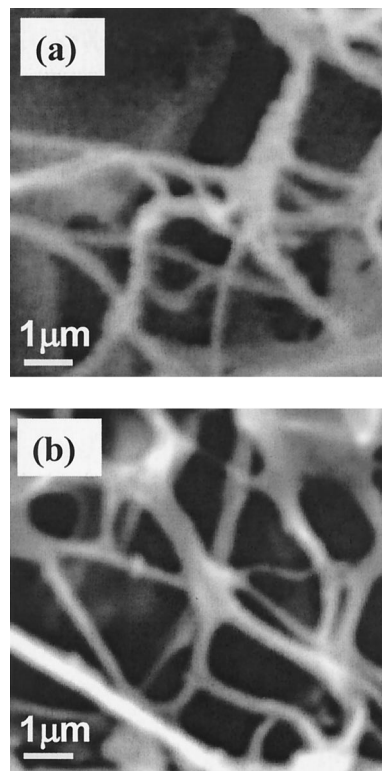


Fig. 2. SEM images of (a) the rat colonic connective tissue and (b) the bioengineered connective tissue model.

tissue and the bioengineered connective tissue model show randomly oriented and interwoven fibers and fiber bundles with similar fiber density. Quantitatively, the diameter of collagen fibers and fiber bundles of the rat colon connective tissue was estimated to range from 300 to 600 nm ( $\sim 500 \pm 90$  nm), and the average spacing between fiber bundles varied from 500 to 1100 nm ( $\sim 840 \pm 300$  nm). For the bioengineered tissue model, the fiber diameter ranged from 250 to 500 nm ( $\sim 470 \pm 100$  nm), and the average spacing fell into the range of 600 to 1000 nm ( $\sim 890 \pm 230$  nm). Therefore the colonic connective tissue and the bioengineered tissue model show similar fiber diameter and density.

The structural similarity between the bioengineered tissue model and the connective tissue is attributed to the fact that they share a common major component—collagen fibers. Collagen fibers are the basic building block of the bioengineered connective tissue model and also the essential structural element present in all kinds of connective tissue.<sup>34</sup> Depending on the portion of the fiber in the connective tissue, connective tissue can be classified as either loose or dense connective tissue. Dense connective tissue consists of either closely packed, roughly parallel bundles or densely packed, irregularly oriented fibers. It is found in the tendons and cartilage.<sup>34</sup> Loose connective tissue consists of loosely interwoven fibers in seemingly random orientation and is found in the mucosa, submucosa, and stroma of the majority of human organs and is the type of connective

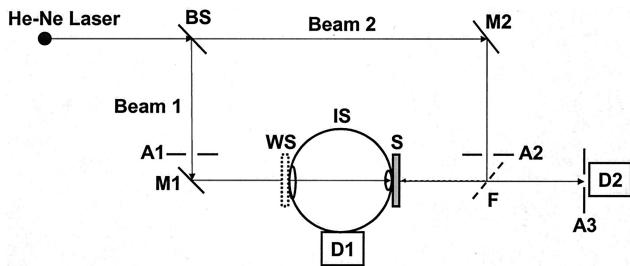


Fig. 3. Design of the integrating-sphere setup. BS, beam splitter; A1, A2, A3, apertures; M1, M2, mirrors; WS, reflectance white standard; IS, integrating sphere; S, sample; F, flipper; D1 and D2, photodiodes.

tissue relevant to the majority of tissue optics applications.<sup>34</sup> Figure 2 illustrates these properties of loose connective tissue. We conclude that, as evident from Fig. 2 and the supporting analyses, the microstructure of our bioengineered connective tissue model is similar to that of loose connective tissue.

#### 4. Characterization of the Optical Properties of the Bioengineered Tissue Model

##### A. Integrating-Sphere Setup

To be suitable for light transport studies, a tissue model must possess optical properties similar to living tissue. In this section we show that our tissue model satisfies this requirement. We assessed the following optical characteristics: the absorption coefficient  $\mu_a$ , the scattering coefficient  $\mu_s$ , the anisotropy factor  $g$ , and the reduced scattering coefficient  $\mu_s'$ ; the last one can be calculated with the equation  $\mu_s' = \mu_s(1 - g)$ , and the optical thickness is defined as  $\tau = (\mu_s + \mu_a)d$ , where  $d$  is the physical depth of a medium. The optical properties were measured with an integrating-sphere instrument in conjunction with the inverse adding–doubling algorithm developed by Prahl.<sup>39</sup> The sphere spatially integrates radiant flux and measures the total reflectance  $R_d$ , total diffuse transmission  $T_d$ , and collimated transmission  $T_c$ . The adding–doubling method provides an accurate solution of the radiative transport equation. The inverse adding–doubling method is a numerical iterative algorithm used to calculate the optical properties  $\mu_a$ ,  $\mu_s$ ,  $\mu_s'$ , and  $g$  from known  $R_d$ ,  $T_d$ , and  $T_c$ . This method has been shown to be highly accurate with an accuracy better than  $\pm 2\%–3\%$ .<sup>40,41</sup>

Figure 3 illustrates the setup of the integrating sphere (IS-060, Labsphere). A He–Ne laser with a 632.8-nm (Melles Griot) or 543.5-nm wavelength (Coherent) was used as the collimated light source. The beam splitter separated the incident light into two beams. For measuring the total reflectance, beam 1 irradiated the sample, and a beam stop was used to block beam 2, whereas, during the measurement of total diffuse transmission, beam 2 was redirected by the flipper F (New Focus), and the beam stop blocked beam 1. The size of the beam was controlled by means of apertures A1 and A2. In our studies the beam was 1 mm in diameter. The total reflectance and the total

diffuse transmission were collected by the photodiode D1 (Newport). The photodiode D2 was positioned 60 cm away from the sample and recorded the collimated transmission intensity. The aperture A3 with a size equal to that of the beam was positioned in front of D2 to minimize the collection of scattered light. The total reflectance, the total diffuse transmission, and collimated transmission were corrected for the dark intensity with the following relations:

$$R_d = \frac{R_s - R_0}{R_{\text{ref}} - R_{\text{ref}0}}$$

$$T_d = \frac{T_s - T_0}{T_{\text{ref}} - T_{\text{ref}0}},$$

$$T_c = \frac{Tc_s - Tc_0}{Tc_{\text{ref}} - Tc_{\text{ref}0}},$$

where  $R_d$ ,  $T_d$ , and  $T_c$  are the total reflectance, total diffuse transmission, and collimated transmission, respectively, and the subscripts 0, ref, and ref0 refer to the sample, dark, reference, and reference dark, respectively.  $R_0$ ,  $T_0$ ,  $Tc_0$ ,  $R_{\text{ref}0}$  and  $T_{\text{ref}0}$  were collected with the incident light blocked by the beam stop;  $R_{\text{ref}}$  and  $T_{\text{ref}}$  were 100% reflectance and transmission, collected with the front port open and the back port replaced by a 99%-reflectance standard plate (SRS-99-010, Labsphere).  $Tc_{\text{ref}}$  was collected as the incident light intensity with no sample present as 100% collimated transmission.

##### B. Experimental Validation of the Accuracy of Integrating-Sphere Measurements

To validate the accuracy of the measurement of the scattering property by means of the integrating-sphere setup in combination with the inverse adding–doubling algorithm, we conducted studies with microsphere suspensions with known scattering properties. The microsphere suspensions were contained in either a 5-mm-path-length quartz cuvette (VWR) or a specially designed sample holder. Polystyrene microspheres (Duke Scientific) of three sizes (0.43, 0.5, and 0.65  $\mu\text{m}$ ) were used, and the optical properties of the suspensions were calculated with Mie theory, which provides the exact solution to the problem of light scattering by isolated uniform spheres of arbitrary sizes. Table 1 shows the comparison between the experimental results obtained with the integrating sphere and those obtained with Mie calculation. As shown in Table 1, the integrating-sphere method permits determination of the scattering coefficient  $\mu_s$ , anisotropy factor  $g$ , and reduced scattering coefficient  $\mu_s'$  with error less than 5% in a wide range of scattering coefficients ranging from 7 to 300  $\text{cm}^{-1}$ . In addition, the accuracy of measurement of the absorption coefficient was also validated with a set of neutral-density filters (Thorlabs) with the known absorption coefficient provided by the manufacturer, and the error of the measured absorption coefficient  $\mu_a$  was found to be below 5%.

**Table 1. Comparison of Optical Properties of Polystyrene Microsphere Suspension between the Experimental Results and Mie Calculation**

Optical Property	Comparison	0.43 $\mu\text{m}$	0.50 $\mu\text{m}$	0.65 $\mu\text{m}$
$\mu_s$ ( $\text{cm}^{-1}$ )	Experiment	$7.06 \pm 0.11$	$9.71 \pm 0.07$	$12.80 \pm 0.07$
	Mie calculation	7.10	9.40	12.80
$g$	Experiment	$0.75 \pm 0.01$	$0.83 \pm 0.01$	$0.87 \pm 0.01$
	Mie calculation	0.76	0.83	0.87
$\mu_s'$ ( $\text{cm}^{-1}$ )	Experiment	$1.69 \pm 0.07$	$1.65 \pm 0.06$	$1.67 \pm 0.08$
	Mie calculation	1.67	1.67	1.67
$\mu_s$ ( $\text{cm}^{-1}$ )	Experiment	$201.47 \pm 5.69$	$103.17 \pm 3.45$	$292.67 \pm 7.09$
	Mie calculation	200.42	99.85	300.45
$g$	Experiment	$0.77 \pm 0.02$	$0.82 \pm 0.01$	$0.87 \pm 0.002$
	Mie calculation	0.76	0.83	0.87
$\mu_s'$ ( $\text{cm}^{-1}$ )	Experiment	$46.38 \pm 1.27$	$18.57 \pm 1.62$	$38.05 \pm 1.56$
	Mie calculation	48.10	16.97	35.06

**C. Optical Properties of Connective Tissue and the Bioengineered Tissue Model**

We used the integrating-sphere technique to determine the optical properties of the bioengineered tissue model, as discussed above. Specifically, for  $\lambda = 632.8 \text{ nm}$ , the scattering coefficient  $\mu_s = 310 \pm 15 \text{ cm}^{-1}$ , anisotropy factor  $g = 0.95 \pm 0.01$ , and the reduced scattering coefficient  $\mu_s' = 15.5 \pm 1.3 \text{ cm}^{-1}$ . To compensate for the inhomogeneity of the tissue model, we took  $n = 8$  measurements for each sample. We found that the optical properties of the tissue model are temporally stable and reproducible with accuracy better than  $\pm 8\%$ .

The optical properties of various biological tissues have been extensively investigated and documented.<sup>42–44</sup> The optical properties vary significantly among different tissue types. Typically, for connective tissue,  $\mu_s$  ranges from 200 to 600  $\text{cm}^{-1}$ ,  $g \sim 0.90\text{--}0.97$ , and  $\mu_s' \sim 10\text{--}25 \text{ cm}^{-1}$ . Given these values, it is evident that all three optical characteristics of the bioengineered tissue model,  $\mu_s$ ,  $g$ , and  $\mu_s'$ , are within the range of values reported for most biological tissues. We conclude that the optical properties of the bioengineered tissue are similar to those of the real biological tissue.

To facilitate the investigation of light transport in tissue, one must vary or control the optical and physical properties of the tissue model in a predictable manner, which is crucial for repeatable and well-characterized experiments. As discussed in Section 2, the optical and physical properties of tissue models can be controlled to cover the physiological range. Using the protocol discussed in Section 2, we were able to reproducibly fabricate the bioengineered tissue models with  $\mu_s$  ranging from 100 to 500  $\text{cm}^{-1}$  and  $g$  ranging from 0.58 to 0.96. The physical thickness of the tissue model can be controlled from 5  $\mu\text{m}$  to 2 mm. (Evidently, models with thickness exceeding 2 mm can also be easily fabricated; however, we did not attempt to develop such models in this study.) Importantly, the optical and physical properties of the tissue model are highly reproducible. As discussed above, the tissue model can be repeatedly made with the standard deviation of the optical and

physical parameters within 8% of their respective means.

**5. Polarization Studies**

One of the major advantages of the bioengineered tissue model is that its physical and optical properties can be reproducibly controlled. This facilitates the experimental investigation of light transport in tissue. In this section, as an example of the application of this bioengineered tissue model to investigate the polarized light propagation in biological tissue, we demonstrate the utilization of the model to study the effect of epithelium and the underlying connective tissue on the depth selectivity of polarization gating.

In polarization gating, the polarized light illuminates the sample, and the returned elastic scattering signal is split into two components with polarizations parallel [copolarized signal ( $I_{\parallel}$ )] and orthogonal [cross-polarized signal ( $I_{\perp}$ )] to that of the incident light. The underlying principle of polarization gating is that light scattered in the superficial tissue retains its original polarization and therefore contributes to  $I_{\parallel}$ , whereas light propagating deep into the tissue is depolarized by means of multiple scattering. Therefore the differential polarization signal,  $\Delta I = I_{\parallel} - I_{\perp}$ , is predominately determined by the light scattering in the superficial portion of the tissue.<sup>12–14,22</sup> However, the penetration depth of the differential polarization signal in biological tissue has not been quantified. In the mucosa the epithelium and connective tissue have distinct morphological and optical properties. The esophageal epithelium is a classic example of the stratified squamous epithelium, which is avascular tissue consisting of approximately ten layers of closely packed and contiguous cells,<sup>45,46</sup> whereas connective tissue consists of randomly oriented collagen fibers and fiber bundles. Such differences in structure translate into significant different optical properties. Therefore the physical and optical depth of epithelial and connective tissues probed by means of polarization gating may be substantially different. Here we investigate the effect of epithelium

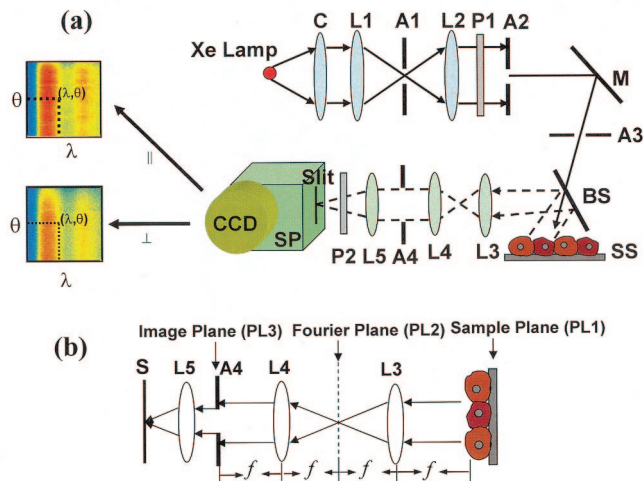


Fig. 4. (a) Schematic of the experimental setup for polarization measurements. C, condenser; L1, L2, L3, L4, L5, lenses; BS, beam splitter; M, mirror; A1, A2, A3, A4, apertures; SS, sample stage; P1, P2, polarizers; SP, imaging spectrograph; CCD, charge-coupled device camera. (b) Unfolded view of the collection arm consisting of a  $4f$  imaging system of L3, L4, and a Fourier lens L5. Lens L3 is positioned at one focal length from the sample plane PL1. The  $4f$  system of L3, L4 projects an image of the sample onto plane PL3. The readable aperture A4 in PL3 is used to control the area of scattered light collection. Lens L5 projects the angular distribution of the scattered light from the area of interest onto the slit (S) of the imaging spectrograph SP.

and connective tissues on the penetration depth of polarization gating.

#### A. Experimental Setup

We developed a specialized instrument to investigate the propagation of polarized light in tissue. This instrument permits collection of comprehensive light-scattering data including the wavelength, angular, and polarization characteristics of scattered light. This instrument also allows control over the illumination and collection areas on a tissue surface. Figure 4(a) shows the schematic of the experimental setup. A beam of broadband cw light from a 500-W xenon lamp (Oriol) was collimated by use of a  $4f$  lens system of L1, L2, and aperture A1 (Newport) (divergence angle  $\sim 0.03^\circ$ ), polarized, and delivered onto a sample of  $15^\circ$  angle of incidence to prevent the collection of the specular reflection. The size of the illumination beam was controlled with aperture A3.

The size of the detection area was controlled by means of a  $4f$  imaging system of L3 and L4 in the light-collection arm of the system [Fig. 4(b)] with lens L3 positioned one focal distance from the sample surface. This  $4f$  system projected an image of the spatial distribution of the scattered light emerging from the sample surface onto plane PL3. Aperture A4 positioned in this image plane selected the collection area of interest. Lens L5 positioned at a focal length from the image plane PL3 projected the angular distribution of the scattered light onto the slit of the imaging spectrometer (SpectraPro-150, Acton Research Corp.) coupled to the charge-coupled device (CCD) (Cool-

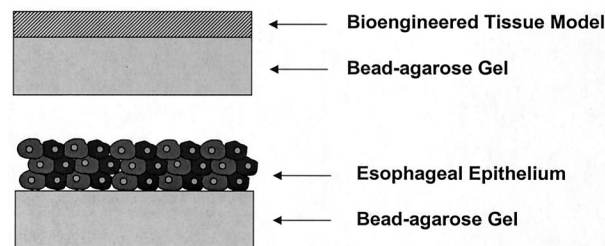


Fig. 5. Schematic of a two-layered tissue phantom. The base layer consists of  $4.78\text{-}\mu\text{m}$  polystyrene microspheres embedded in an agarose gel. The top layer consists of either the bioengineered connective tissue model or the rat esophageal squamous stratified epithelium.

SnapHQ, Roper Scientific). The imaging spectrograph dispersed this light now in the direction orthogonal to the slit according to its spectral composition. Thus the instrument recorded a matrix of the distribution of scattered light intensity as a function of wavelength (from 400 to 700 nm) and angle of scattering (within  $\pm 5^\circ$  from the backward direction). In this matrix, one axis corresponded to the wavelength of light, and the other corresponded to the angle of scattering for a fixed polarization and the azimuth of scattering (i.e., the polar angle of the direction of light propagation with respect to the direction of polarization). We selected the azimuth of scattering by rotating the polarizer in the delivery arm of the system.

The combination of the linear polarizers P1 and P2 in the delivery and collection arms of the system, respectively, allowed measurement of the two independent polarization components of the light scattered from the sample: the intensity of the scattered light polarized along the direction of polarization of the incident light, i.e., the copolarized component  $I_{\parallel}$ , and the intensity of the scattered light polarized orthogonally to the polarization of the incident light, i.e., the cross-polarized component  $I_{\perp}$ . To compensate for the nonuniform spectral profile of the light source and other artifacts, we normalized the light-scattering intensity maps by those measured from a 99%-reflectance white standard (SRS-99-010, Labsphere). The instrument was calibrated and tested by use of a conventional protocol in experiments with physical tissue models, which consisted of suspensions of polystyrene microspheres of sizes ranging from 0.2 to  $10\ \mu\text{m}$ . The light-scattering data recorded in these experiments were found to be in excellent agreement with the predictions of Mie theory, which provides the exact solution to the light scattering by spheres.<sup>11</sup>

#### B. Concept of Polarization Measurements in Two-Layered Tissue Models

To study the effects of epithelium and the underlying connective tissue on the depth of tissue probed by use of polarization gating, i.e., the differential polarization signal  $\Delta I$ , we used two-layered tissue models (Fig. 5). The bioengineered connective tissue and rat esophageal epithelium were used as models of con-

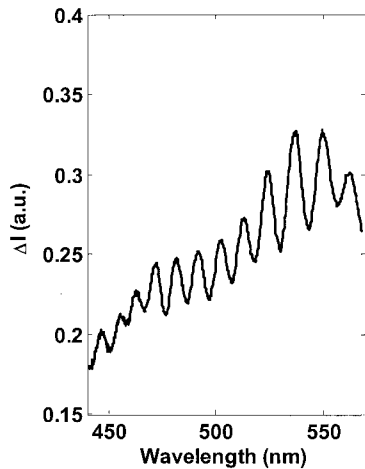


Fig. 6. Spectrum of light scattered by 4.78- $\mu\text{m}$  microspheres exhibits a characteristic feature: high-frequency oscillations of intensity as a function of wavelength.

nective and squamous stratified epithelial tissues, respectively, and formed the first (top) layer in the two-layered phantom. The second (base) layer contained a suspension of 4.78- $\mu\text{m}$  polystyrene. The spectra of light scattered by such resonant-size microspheres exhibit a characteristic feature: high-frequency oscillations of intensity as a function of wavelength (Fig. 6). As discussed below, we used this property to distinguish between photons penetrating into the base and those trapped in the top layer.

Conceptually, the experiments with two-layered tissue phantoms were designed as follows: In the case in which the superficial layer is sufficiently thin and a substantial portion of photons contributing to differential polarization signals  $\Delta I$  propagates through the top layer into the base, the differential polarization spectrum must exhibit the characteristic scattering feature of the base layer, i.e., the high-frequency wavelength-dependent oscillatory component in the spectrum of the resulting scattered signal (Fig. 6). On the other hand, if all differential polarization photons are localized within the top layer, the differential polarization intensity spectrum should not exhibit the high-frequency oscillation. Thus, by varying the thickness of the top layer, one can use the unique high-frequency oscillation feature to quantify the depth probed with polarization gating.

### C. Fabrication of Two-Layered Tissue Models

First, as a comparison with the connective tissue, we investigated the optical properties of the epithelial tissue. For preparing the epithelial tissue sample, eight Fisher 344 rats were sacrificed, and their esophagi were removed. The esophageal epithelium was carefully peeled out with forceps and separated from the connective tissue following a standard procedure.<sup>47</sup> To confirm the isolation of the epithelium (i.e., the lack of residual connective tissue underlying the epithelium), we used a visual inspection of the tissue (in a sharp contrast to avascular epithelium, which consists of continuous epithelial cells, the esophageal

connective tissue is vascular, which results in a visible color difference between these two tissue types), followed by the histological examination of hemotoxylin and eosin (H&E) stained tissue sections obtained from different parts of the separated epithelium. The histology images revealed no connective tissue underneath the separated epithelial layer. The epithelium was kept in the 1 $\times$  phosphate-buffered saline immediately after its removal. All measurements were taken within 2 h after the procedure. The thickness of esophageal tissue had intrinsic variations depending on the location along the esophagus, with optical thickness ranging from  $\sim 0.3$  to  $\sim 5$  and physical thickness varying from  $\sim 50$  to  $\sim 700$   $\mu\text{m}$ . The tissue was mounted between two ultrathin coverslips. We measured the optical thickness with the integrating-sphere setup in conjunction with the inverse adding-doubling algorithm. The physical thickness was measured by means of a caliper, which is a standard technique commonly used by several investigators.<sup>30,48</sup> The optical properties of the epithelial tissue samples were measured with the integrating-sphere technique as discussed in Subsection 4.A, and the following values were obtained for  $\lambda = 632.8$  nm:  $\mu_s = 58.9 \pm 2.3$   $\text{cm}^{-1}$ ,  $g = 0.94 \pm 0.01$ , and  $\mu_s' = 3.46 \pm 0.2$   $\text{cm}^{-1}$ . We point out that the scattering coefficient of the bioengineered connective tissue model as well as connective tissue is approximately five times greater than that of epithelium. Collier and colleagues reported similar results for cervical tissue.<sup>49</sup>

The second (base) layer was prepared as a solid phantom consisting of a suspension of 4.78- $\mu\text{m}$  polystyrene microspheres (2% by weight) (Polysciences) embedded in an agarose gel (2 g of agarose per 100 ml of distilled water). The spectra of light scattered by such resonant-size microspheres exhibit a well-known, characteristic, and unique feature: high-frequency oscillations of intensity as a function of wavelength (Fig. 6). The geometrical and optical thicknesses of the base layer were  $d = 5$  mm and  $\tau = 60$ , respectively (in our study,  $\mu_a = 0$  and optical thickness  $\tau = \mu_s d$ ). The optical properties of the base layer were comparable with those of mucosal-submucosal tissue ( $\mu_s = 120$   $\text{cm}^{-1}$  and  $\mu_a = 0.1$   $\text{cm}^{-1}$  at 632.8 nm). The optical property of the base layer was first calculated on the basis of Mie theory and then experimentally confirmed with the integrating-sphere setup in combination with the inverse adding-doubling algorithm as we discussed in Subsection 4.A.

### D. Polarization Measurements in Two-Layered Tissue Phantoms

To compare the effect of epithelium and connective tissue on polarization gating, we varied optical thickness  $\tau$  of the top layer (either the epithelium or the connective tissue model) by selecting samples of various physical thicknesses. The optical thickness of the top layer was varied from 0 to  $\sim 6$ –8. Signals  $I_{\parallel}$ ,  $I_{\perp}$ , and  $\Delta I = I_{\parallel} - I_{\perp}$  were recorded for the azimuthal

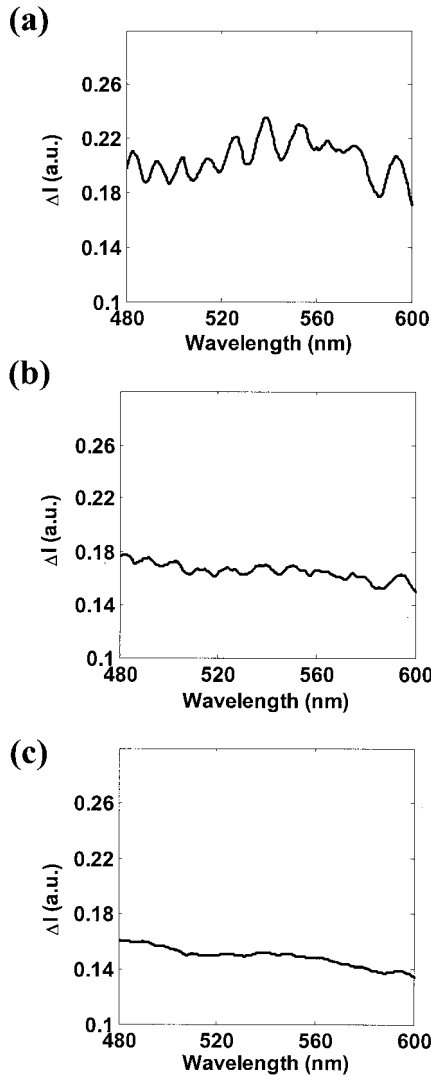


Fig. 7. Spectrum of differential polarization signal  $\Delta I(\lambda)$  for various values of the optical thickness of the superficial layer in a two-layered tissue phantom. (a) For optical thickness  $\tau = 0$  (no superficial layer),  $\Delta I(\lambda)$  shows the characteristic scattering feature of the base layer, i.e., the high-frequency oscillations in wavelength. (b) As  $\tau$  increases ( $\tau \sim 1.2$ ), the high-frequency oscillations decrease, thus indicating that more differential polarization photons are localized within the top layer. (c) When the optical thickness of the superficial layer  $\tau$  is increased further ( $\tau \sim 3$ ), the high-frequency oscillations in  $\Delta I(\lambda)$  vanish. At this point, the majority of differential polarization photons are localized within the top layer.

angle  $0^\circ$  and the illumination and collection areas 2 and 5 mm in diameter, respectively.

Figure 7 demonstrates the spectrum of differential polarization signal  $\Delta I$  for different optical thicknesses of the superficial layer consisting of an esophageal epithelium. For  $\tau = 0$  (no superficial layer), the spectrum of  $\Delta I$  shows the characteristic oscillatory scattering feature of the base layer. In our experiment, we gradually increased the optical thickness  $\tau$  of the superficial layer while keeping the other optical properties constant. As shown in Fig. 7, as  $\tau$  increases, the amplitude of the high-frequency oscillations de-

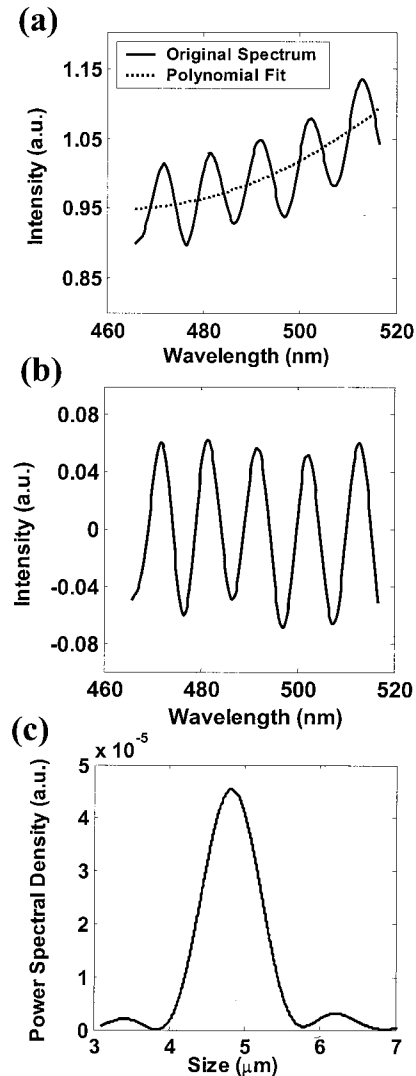


Fig. 8. Schematic illustrating the algorithm to quantify the contribution of a top phantom layer to the differential polarization signal at each optical depth. (a) A differential polarization spectrum is mean scaled. Then a second-order polynomial is used to fit the normalized differential polarization signal. (b) The fit shown in (a) is subtracted from the original signal to extract the high-frequency component. (c) The power spectrum density of the high-frequency component is evaluated at the respective size.

creases, thus indicating that more differential polarization photons are localized within the top layer. Eventually, for a sufficiently thick top layer,  $\tau \sim 3$ , the high-frequency oscillations in  $\Delta I(\lambda)$  vanish. At this point, the majority of differential polarization photons are localized within the top layer, and only a negligible portion of light contributing to  $\Delta I$  penetrates into the base layer.

To quantify the contribution of each phantom layer to the differential polarization signal at each optical depth, we developed an algorithm illustrated in Fig. 8. First, a differential polarization spectrum was mean scaled. Then a second-order polynomial was used to fit the normalized differential polarization signal as shown in Fig. 8(a). This fit was subtracted

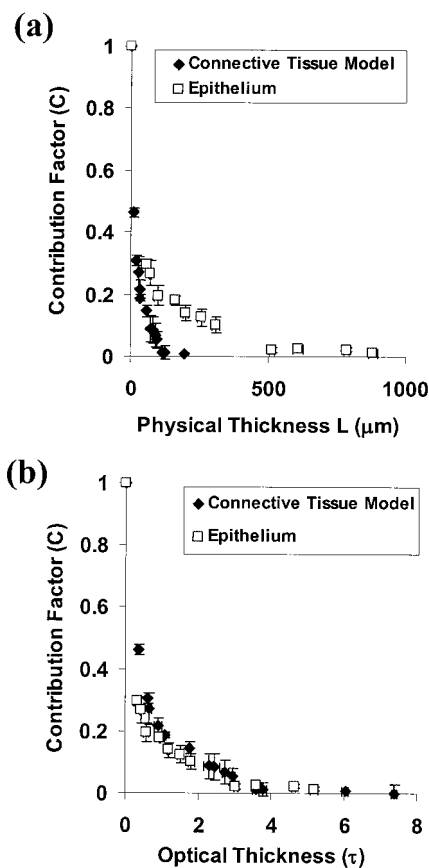


Fig. 9. (a) Contribution factor  $C$  as a function of the physical thickness of the bioengineered connective tissue model (diamonds) and epithelium (squares). (b) Contribution factor  $C$  as a function of the optical thickness  $\tau$  of either the bioengineered connective tissue model (diamonds) or esophageal epithelium (squares).  $C(\tau)$  quantifies the portion of the differential polarization signal contributed from tissue depths greater than  $\tau$ .

from the original signal to extract the high-frequency components [Fig. 8(b)]. The amplitude of the high-frequency component  $A$  was quantified by means of the Fourier analysis as the square root of the power spectrum density of the high-frequency component evaluated at the respective size [Fig. 8(c)]. The resulting coefficient, referred to hereafter as the contribution factor  $C$ , was normalized to 1 at zero optical thickness of the top layer. Thus  $0 \leq C \leq 1$ . The contribution factor  $C(\tau)$  quantifies the portion of the differential polarization signal contributed from tissue depths greater than  $\tau$ .  $C = 1$  corresponds to the case in which the differential polarization signal is completely contributed by the base layer, whereas  $C = 0$  indicates that the differential polarization signal originates from the top layer.

## E. Results and Discussion

Figure 9(a) shows the contribution factor as a function of the physical thickness  $L$  of the bioengineered connective tissue model,  $C_C(L)$ , and epithelium,  $C_E(L)$ . At each thickness, several measurements were taken ( $n \geq 6$ ), and the mean value and standard

deviation of the contribution factor were calculated. For both tissue types, the contribution factor rapidly decreases with thickness, indicating that the differential polarization signal is rapidly localized within the top layer and contributed by short traveling photons. However, as shown in Fig. 9(a), the decline is more precipitant for connective tissue. This demonstrates that the physical penetration depth reached by the differential polarization signal in the epithelium is approximately six to seven times longer than that in the connective tissue. For example, if the differential polarization signal probes the top  $\sim 200$ – $300$   $\mu\text{m}$  in the squamous stratified epithelium, the penetration depth in connective tissue is only  $\sim 40$ – $50$   $\mu\text{m}$ .

We hypothesized that such a difference in the penetration depth is due to the higher scattering coefficient of connective tissue compared with that of the epithelium. To test this hypothesis, we investigated the dependence of  $C$  on the optical thickness  $\tau$  of epithelial and connective tissues. Here optical thickness  $\tau$  is defined as the product of scattering coefficient  $\mu_s$  and physical thickness  $d$  ( $\mu_a = 0$ ). (Light traversing a medium with  $\tau = 1$  undergoes, on average, one scattering event.) Figure 9(b) shows the contribution factor as a function of the optical thickness of either the bioengineered connective tissue model,  $C_C(\tau)$ , or the esophageal epithelium,  $C_E(\tau)$ . As evident from Fig. 9(b),  $C_C(\tau)$  matches  $C_E(\tau)$  for  $\tau < 7.8$ . Despite the fact that epithelium and connective tissue have substantial intrinsic differences in structure and scattering properties, their contributions to the differential polarization signal mainly depend on the optical thickness.

Figure 9(b) also shows that more than 90% of the differential polarization signal is contributed from the superficial tissue up to  $\tau < 2$ . The corresponding physical depth depends on the tissue type. In particular, in mucosal tissue the thickness of the epithelium may vary significantly. For example, the mucosae of the colon and Barrett's esophagus are covered by a single-cell-layer columnar epithelium,  $\sim 20$ – $30$   $\mu\text{m}$  thick. In such tissue the optical thickness of the epithelium is typically less than 1 and  $\tau = 2$  includes both the epithelium and the underlying connective tissue. Thus polarization gating may probe the entire thickness of the epithelium plus a portion of the connective tissue. On the other hand, the mucosae of the skin and uterine cervix consist of a relatively thick multilayered squamous stratified epithelium, which can be several hundreds of micrometers thick. In such tissue the optical thickness of the epithelium may exceed 2, and the differential polarization signal may be contributed by the epithelial layer alone with only negligible contribution from the underlying stroma.

## 6. Conclusions

We report the development of a bioengineered connective tissue model that shows a great similarity to the real connective tissue in both its microstructure and its optical properties. The physical and optical

properties of the model are temporally stable and can be reproducibly controlled, which makes this tissue model particularly convenient for experimental investigation of light propagation and transport in biological tissue. We demonstrated the application of this tissue model in our investigation of the depth sensitivity of polarization gating. Specifically, we studied the effects of epithelium and connective tissue on the depth of penetration of differential polarization signals. Our results indicate that the penetration depth in both epithelial and connective tissues primarily depends on the optical thickness of the tissue: The polarization-gated signal probes the superficial layer of tissue up to the optical depth of  $\sim 2$ . The corresponding physical penetration depth depends on the specific tissue type and in the connective tissue is approximately six to seven times shorter than in the epithelium ( $\sim 40$ – $50$  and  $\sim 200$ – $300$   $\mu\text{m}$ , respectively).

This study was supported in part by National Institutes of Health grant R01CA097966-01 and National Science Foundation grant BES-0238903. We thank Ramesh K. Wali and Hemant K. Roy for providing us the rats. We also thank Jian Yang, Guillermo Ameer, and Xu Li for helpful discussions and Scott Prahl for making the inverse adding–doubling source code publicly available.

## References

1. R. R. Anderson, "Polarized-light examination and photography of the skin," *Arch. Dermatol.* **127**, 1000–1005 (1991).
2. V. Backman, V. Gopal, M. Kalashnikov, K. Badizadegan, R. Gurjar, A. Wax, I. Georgakoudi, M. Mueller, C. W. Boone, R. R. Dasari, and M. S. Feld, "Measuring cellular structure at sub-micrometer scale with light scattering spectroscopy," *IEEE J. Sel. Top. Quantum Electron.* **7**, 887–893 (2001).
3. I. Georgakoudi, B. C. Jacobson, J. Van Dam, V. Backman, M. B. Wallace, M. G. Muller, Q. Zhang, K. Badizadegan, D. Sun, G. A. Thomas, L. T. Perelman, and M. S. Feld, "Fluorescence, reflectance, and light-scattering spectroscopy for evaluating dysplasia in patients with Barrett's esophagus," *Gastroenterology* **120**, 1620–1629 (2001).
4. M. Bartlett, G. Huang, L. Larcom, and H. B. Jiang, "Measurement of particle size distribution in mammalian cells *in vitro* by use of polarized light spectroscopy," *Appl. Opt.* **43**, 1296–1307 (2004).
5. J. R. Mourant, I. J. Bigio, J. Boyer, R. L. Conn, T. Johnson, and T. Shimada, "Spectroscopic diagnosis of bladder cancer with elastic light scattering," *Lasers Surg. Med.* **17**, 350–357 (1995).
6. A. E. Cerussi, D. Jakubowski, N. Shah, F. Bevilacqua, R. Lanning, A. J. Berger, D. Hsiang, J. Butler, R. F. Holcombe, and B. J. Tromberg, "Spectroscopy enhances the information content of optical mammography," *J. Biomed. Opt.* **7**, 60–71 (2002).
7. A. Wax, C. H. Yang, M. G. Muller, R. Nines, C. W. Boone, V. E. Steele, G. D. Stoner, R. R. Dasari, and M. S. Feld, "*In situ* detection of neoplastic transformation and chemopreventive effects in rat esophagus epithelium using angle-resolved low-coherence interferometry," *Cancer Res.* **63**, 3556–3559 (2003).
8. K. Sokolov, R. Drezek, K. Gossage, and R. Richards-Kortum, "Reflectance spectroscopy with polarized light: is it sensitive to cellular and nuclear morphology," *Opt. Express* **5**, 302–317 (1999).
9. L. Nieman, A. Myakov, J. Aaron, and K. Sokolov, "Optical sectioning using a fiber probe with an angled illumination-collection geometry: evaluation in engineered tissue phantoms," *Appl. Opt.* **43**, 1308–1319 (2004).
10. J. R. Mourant, T. M. Johnson, S. Carpenter, A. Guerra, T. Aida, and J. P. Freyer, "Polarized angular dependent spectroscopy of epithelial cells and epithelial cell nuclei to determine the size scale of scattering structures," *J. Biomed. Opt.* **7**, 378–387 (2002).
11. Y. Kim, Y. Liu, R. K. Wali, H. K. Roy, M. J. Goldberg, A. K. Kromine, K. Chen, and V. Backman, "Simultaneous measurement of angular and spectral properties of light scattering for characterization of tissue microarchitecture and its alteration in early precancer," *IEEE J. Sel. Top. Quantum Electron.* **9**, 243–257 (2003).
12. S. L. Jacques, J. C. Ramella-Roman, and K. Lee, "Imaging skin pathology with polarized light," *J. Biomed. Opt.* **7**, 329–340 (2002).
13. S. L. Jacques, J. R. Roman, and K. Lee, "Imaging superficial tissues with polarized light," *Lasers Surg. Med.* **26**, 119–129 (2000).
14. V. Backman, R. Gurjar, K. Badizadegan, L. Itzkan, R. R. Dasari, L. T. Perelman, and M. S. Feld, "Polarized light scattering spectroscopy for quantitative measurement of epithelial cellular structures *in situ*," *IEEE J. Sel. Top. Quantum Electron.* **5**, 1019–1026 (1999).
15. V. Backman, M. B. Wallace, L. T. Perelman, J. T. Arendt, R. Gurjar, M. G. Muller, Q. Zhang, G. Zonios, E. Kline, T. McGilican, S. Shapshay, T. Valdez, K. Badizadegan, J. M. Crawford, M. Fitzmaurice, S. Kabani, H. S. Levin, M. Seiler, R. R. Dasari, I. Itzkan, J. Van Dam, and M. S. Feld, "Detection of preinvasive cancer cells," *Nature* **406**, 35–36 (2000).
16. R. S. Gurjar, V. Backman, L. T. Perelman, I. Georgakoudi, K. Badizadegan, I. Itzkan, R. R. Dasari, and M. S. Feld, "Imaging human epithelial properties with polarized light-scattering spectroscopy," *Nat. Med.* **7**, 1245–1248 (2001).
17. L. T. Perelman, V. Backman, M. Wallace, G. Zonios, R. Manoharan, A. Nusrat, S. Shields, M. Seiler, C. Lima, T. Hamano, I. Itzkan, J. Van Dam, J. M. Crawford, and M. S. Feld, "Observation of periodic fine structure in reflectance from biological tissue: a new technique for measuring nuclear size distribution," *Phys. Rev. Lett.* **80**, 627–630 (1998).
18. T. M. Johnson and J. R. Mourant, "Polarized wavelength-dependent measurements of turbid media," *Opt. Express* **4**, 200–216 (1999).
19. H. K. Roy, Y. Liu, R. K. Wali, Y. Kim, M. J. Goldberg, A. K. Kromine, and V. Backman, "Four-dimensional elastic light scattering fingerprints as preneoplastic markers in the rat model of colon carcinogenesis," *Gastroenterology* **126**, 1071–1081 (2004).
20. A. Amelink, H. Sterenborg, M. P. L. Bard, and S. A. Burgers, "*In vivo* measurement of the local optical properties of tissue by use of differential pathlength spectroscopy," *Opt. Lett.* **29**, 1087–1089 (2004).
21. S. A. Boppart, B. E. Bouma, C. Pitris, J. F. Southern, M. E. Brezinski, and J. G. Fujimoto, "*In vivo* cellular optical coherence tomography imaging," *Nat. Med.* **4**, 861–865 (1998).
22. S. G. Demos and R. R. Alfano, "Optical polarization imaging," *Appl. Opt.* **36**, 150–155 (1997).
23. J. A. Izatt, M. D. Kulkarni, H. W. Wang, K. Kobayashi, and M. V. Sivak, "Optical coherence tomography and microscopy in gastrointestinal tissues," *IEEE J. Sel. Top. Quantum Electron.* **2**, 1017–1028 (1996).
24. S. Jiao, G. Yao, and L. Wang, "Depth-resolved two-dimensional Stokes vectors of backscattered light and Mueller matrices of biological tissue measured with optical coherence tomography," *Appl. Opt.* **39**, 6318–6324 (2000).
25. Y. L. Kim, Y. Liu, V. M. Turzhitsky, H. K. Roy, R. K. Wali, and

- V. Backman, "Coherent backscattering spectroscopy," *Opt. Lett.* **29**, 1906–1908 (2004).
26. Q. Liu and N. Ramanujam, "Experimental proof of the feasibility of using angled fiber-optic probe for depth-sensitive fluorescence spectroscopy of turbid media," *Opt. Lett.* **29**, 2034–2036 (2004).
  27. V. V. Tuchin, *Handbook of Optical Biomedical Diagnostics* (SPIE Press, Bellingham, Wash., 2002), pp. 312–352.
  28. V. Sankaran, M. J. Everett, D. J. Maitland, and J. T. Walsh, "Comparison of polarized-light propagation in biological tissue and phantoms," *Opt. Lett.* **24**, 1044–1046 (1999).
  29. V. Sankaran, J. T. Walsh, and D. J. Maitland, "Polarized light propagation through tissue phantoms containing densely packed scatterers," *Opt. Lett.* **25**, 239–241 (2000).
  30. V. Sankaran, J. T. Walsh, and D. J. Maitland, "Comparative study of polarized light propagation in biologic tissues," *J. Biomed. Opt.* **7**, 300–306 (2002).
  31. K. Sokolov, J. Galvan, A. Myakov, A. Lacy, R. Lotan, and R. Richards-Kortum, "Realistic three-dimensional epithelial tissue phantoms for biomedical optics," *J. Biomed. Opt.* **7**, 148–156 (2002).
  32. A. Zoumi, A. Yeh, and B. J. Tromberg, "Imaging cells and extracellular matrix *in vivo* by using second-harmonic generation and two-photon excited fluorescence," *Proc. Natl. Acad. Sci. USA* **99**, 11014–11019 (2002).
  33. G. Marquez, L. V. Wang, C. J. Wang, and Z. B. Hus, "Development of tissue-simulating optical phantoms: poly-*N*-isopropylacrylamide solution entrapped inside a hydrogel," *Phys. Med. Biol.* **44**, 309–318 (1999).
  34. W. Bloom, D. W. Fawcett, and A. A. Maximow, *A Textbook of Histology*, 10th ed. (Saunders, Philadelphia, 1975), pp. 133–167.
  35. E. Sachlos and J. T. Czernuszka, "Making tissue engineering scaffolds work. Review on the application of solid freeform fabrication technology to the production of tissue engineering scaffolds," *Eur. Cells Mater.* **5**, 29–40 (2003).
  36. M. A. Hayat, *Principles and Techniques of Electron Microscopy: Biological Applications*, 3rd ed. (CRC Press, Boca Raton, Fla., 1989).
  37. A. Boyde, E. Bailey, S. J. Jones, and A. Tamarin, "Dimensional changes during specimen preparation for scanning electron microscopy," *Scanning Electron Microsc.* **1**, 507–518 (1977).
  38. A. Boyde and F. Franc, "Freeze-drying shrinkage of glutaraldehyde-fixed liver," *J. Microsc. (Oxford)* **122**, 75–86 (1981).
  39. S. A. Prahl, "Optical property measurements using the inverse adding–doubling program," (Oregon Medical Laser Center, St. Vincent Hospital, 9205 S. W. Barnes Road, Portland, Ore. 97225), <http://omlc.ogi.edu/software/iad/>, January 1999.
  40. S. A. Prahl, M. J. C. van Gemert, and A. J. Welch, "Determining the optical properties of turbid media by using the adding–doubling method," *Appl. Opt.* **32**, 559–568 (1993).
  41. J. W. Pickering, S. A. Prahl, N. Vanwieringen, J. F. Beek, H. Sterenberg, and M. J. C. Vangemert, "Double-integrating-sphere system for measuring the optical-properties of tissue," *Appl. Opt.* **32**, 399–410 (1993).
  42. A. J. Welch and M. J. C. Vangemert, *Optical-Thermal Response of Laser-Irradiated Tissue* (Plenum, New York, 1995).
  43. J. F. Beek, P. Blokland, P. Posthumus, M. Aalders, J. W. Pickering, H. Sterenberg, and M. J. C. vanGemert, "In vitro double-integrating-sphere optical properties of tissues between 630 and 1064 nm," *Phys. Med. Biol.* **42**, 2255–2261 (1997).
  44. W. F. Cheong, S. A. Prahl, and A. J. Welch, "A review of the optical properties of biological tissues," *IEEE J. Quantum Electron.* **26**, 2166–2185 (1990).
  45. L. P. Gartner and J. L. Hiatt, *Color Atlas of Histology*, 2nd ed. (Williams and Wilkins, Baltimore, Md., 1994), pp. 260–261.
  46. W. Bloom, D. W. Fawcett, and A. A. Maximow, *A Textbook of Histology*, 10th ed. (Saunders, Philadelphia, Pa., 1994).
  47. K. A. Warfel and M. T. Hull, "Scanning electron microscopic study of the epithelial–mesenchymal junction of the esophagus," *Scanning Electron Microsc.* **Pt 2**, 697–701 (1984).
  48. R. C. Lin, M. A. Shure, A. M. Rollins, J. A. Izatt, and D. Huang, "Group index of the human cornea at 1.3-mm wavelength obtained *in vitro* by optical coherence domain reflectometry," *Opt. Lett.* **29**, 83–85 (2004).
  49. T. Collier, D. Arifler, A. Malpica, M. Follen, and R. Richards-Kortum, "Determination of epithelial tissue scattering coefficient using confocal microscopy," *IEEE J. Sel. Top. Quantum Electron.* **9**, 307–313 (2003).